AJNR

The role of ferritin and hemosiderin in the MR appearance of cerebral hemorrhage: a histopathologic biochemical study in rats.

K R Thulborn, A G Sorensen, N W Kowall, A McKee, A Lai, R C McKinstry, J Moore, B R Rosen and T J Brady

AJNR Am J Neuroradiol 1990, 11 (2) 291-297
http://www.ajnr.org/content/11/2/291

The Role of Ferritin and Hemosiderin in the MR Appearance of Cerebral Hemorrhage: A Histopathologic Biochemical Study in Rats

Keith R. Thulborn[1]
A. Gregory Sorensen[1]
Neil W. Kowall[2]
Ann McKee[2]
Albert Lai[1]
Robert C. McKinstry[1]
John Moore[1]
Bruce R. Rosen[1]
Thomas J. Brady[3]

A rat model of cerebral hemorrhage using stereotaxic injection of blood into the right basal ganglia was developed to investigate the influence of iron metabolism on the appearance of cerebral hemorrhage on MR images. Images of in vitro fixed brain sections stained specifically for different iron-storage substances, ferritin and hemosiderin, created by digitization of the pathology sections using an Eikonix CCD camera, were compared with the in vivo MR images of late-phase hematomas. Areas of the pathologic and MR features of the lesions were quantitatively correlated. The single-slice MR images were obtained with the use of T1- and T2-weighted spin-echo pulse sequences, as well as T2-weighted spin-echo pulse sequences in which the 180° refocusing pulse was offset from the center of the echo time; this was termed an asymmetric spin-echo pulse sequence. The symmetric and asymmetric T2-weighted images allowed the calculation of line-width images, which emphasize line broadening from intravoxel magnetic field inhomogeneities that arise from the presence of iron-containing substances.

From biochemical and histochemical staining, we conclude that at least two iron-storage substances are present in the late phase of resolving cerebral hematomas. Ferritin has a wider distribution than hemosiderin, showing a similar distribution to the MR signal changes of the calculated line-width images. Line-width mapping is a sensitive means of detecting magnetic field inhomogeneities caused by the magnetic susceptibility differences introduced by the aggregation of these iron-storage substances.

***AJNR* 11:291–297, March/April 1990; *AJR* 154: May 1990**

The temporally varying appearance of cerebral hemorrhage observed by MR imaging has been well documented over the full range of magnetic field strengths available for clinical studies [1–8]. Because of the great variability in appearance, hemorrhage has received considerable attention in the clinical literature. The current model developed to rationalize this behavior is that of Gomori and Grossman [1], in which the major features of resolving intraparenchymal cerebral hematoma have been attributed to iron metabolism and integrity of the erythrocyte, as well as to vasogenic edema and structural changes around the site of hemorrhage. This model is an excellent summary of the MR features of cerebral hemorrhage and allows the formulation of several hypotheses that can be tested readily. Specifically pertinent to this investigation, the model states that the signal loss of late-phase hemorrhage on T2-weighted MR images is due to the magnetic susceptibility effects of hemosiderin, an iron-storage substance in macrophages in the periphery of resolving hematomas. Hemosiderin is readily demonstrated by Perls Prussian blue iron stain, used routinely to demonstrate the presence of iron in pathologic specimens. However, on the basis of the biochemistry of iron metabolism, iron storage in the form of ferritin would be expected to be present [9–13]. The purpose of this study was to determine if ferritin makes a contribution to the magnetic susceptibility effects that dominate the MR appearance of resolving hemorrhage in a rat model and to examine the application of line-width mapping, as determined

Received May 14, 1989; revision requested May 23, 1989; final revision received September 5, 1989; accepted September 8, 1989.

Presented at the annual meeting of the American Roentgen Ray Society, New Orleans, May 1989. Winner of the 1989 ARRS Executive Council Award.

This work was supported by U.S. Public Health Service grants 1PO1CA48729, R01CA40303, and T32CA09502 and the General Electric Corp.

[1] Department of Radiology, Massachusetts General Hospital, Fruit St., Boston, MA 02114. Address reprint requests to K. R. Thulborn, Massachusetts General Hospital MR Imaging Center, Second Floor, 13th St., Bldg. 149, Charlestown, MA 02129.

[2] Department of Pathology, Massachusetts General Hospital, Boston, MA 02114.

[3] Department of Medicine, Massachusetts General Hospital, Boston, MA 02114.

0195-6108/90/1102-0291

from symmetric (SE) and asymmetric (ASE) spin-echo pulse sequences, for detection of such magnetic susceptibility effects. Although magnetic susceptibility effects are detected by changes on T2-weighted images, as discussed in detail elsewhere [12, 14, 15], line-width maps have not been used extensively for in vivo studies [16]. The significance of this study is that the magnetic susceptibility effects in the model of Gomori and Grossman [1] of late-phase resolving cerebral hematomas should include ferritin and hemosiderin, thereby bringing the model into agreement with current concepts of iron metabolism.

Materials and Methods

Rat Model of Cerebral Hemorrhage

Three series of rats were prepared in an identical fashion; each series was divided between blood-injected and plasma-injected groups. The two groups of animals were used to isolate the effects attributable to the presence of the injected erythrocytes from effects due to the trauma of injection. The first series was used for MR imaging (blood-injected, $n = 8$; plasma-injected, $n = 2$), the second series for biochemical assays (blood-injected, $n = 14$; plasma-injected, $n = 10$), and the third series for histochemical staining (blood-injected, $n = 9$; plasma-injected, $n = 9$).

Sprague-Dawley male rats (200–250 g, Charles River Breeding Labs., Inc., Wilmington, MA) were placed under general anesthesia by intraperitoneal injection of pentobarbital (60 mg/kg). Animals were numbered by tattoos on entry into the study to identify subsequent MR data files, biochemical samples, and histopathologic specimens. A left carotid arterial or femoral venous catheter was placed in a donor animal using standard cutdown procedures and aseptic technique. The recipient animal was positioned in a stereotaxic frame, and, using aseptic technique, a longitudinal skin incision was made along the dorsal cranium exposing the bregma of the calvarium. A burr hole over the right caudate nucleus (0.5 mm anterior, 3.5 mm lateral) was drilled with an electric drill mounted on the stereotaxic frame [17]. The drill was cooled with sterile lidocaine solution (1%). Care was taken not to penetrate deeper than the inner table of the skull. The stereotaxically mounted sterile syringe (1-ml, 27-gauge needle) was then lowered through the burr hole to the appropriate depth (4.5 mm) [17].

Injection of blood or plasma (0.05 ml) was made at 100 mm Hg pressure by a reproducible mechanical pressure delivered by a weight falling from a constant precalibrated height. This pressure is the mean arterial blood pressure, mimicking arterial hemorrhage. The blood was obtained from the arterial or venous catheter and used within 2 min without heparinization. Hematocrits were determined on all samples of blood to ensure no hemodilution occurred among injected samples (40–45%). The reproducibility of the injection technique was verified initially by the similar histopathologic appearances and sizes of the acute lesions in animals sacrificed within 12 hr after production of the lesions and by physiologic stability among animals ($n = 6$). Plasma was obtained as the supernatant after centrifugation of heparinized arterial blood (2000 rpm, 3 min, bench centrifuge) and was injected under conditions identical to that of the whole blood. The needle was removed slowly and the burr hole was plugged with bone wax. The scalp incision was closed with sutures after topical administration of bacitracin.

The recipient animals were permitted to recover from anesthesia under warming lights and returned to the animal housing facilities until the imaging procedure. Animals were housed with access to fresh water and rat chow ad lib until sacrifice at 10–100 days. Immediately before imaging, a small glass disk (3 mm diameter × 1 mm thick) containing gadolinium-doped water (1 mmol/l) was glued over the burr hole in the cranium of the rat to allow the lesion to be readily located on the MR images. Imaging was performed within several hours after placement of the marker. Animals were sacrificed by lethal dose of pentobarbital immediately after imaging; the brains were removed intact for further processing, depending on the series. The authors complied with the National Institutes of Health guidelines for use of laboratory animals.

MR Imaging

Procedure.—The blood-injected ($n = 8$) and plasma-injected ($n = 2$) animals in the MR group were imaged 10–15 weeks after injection. Each rat was placed in the prone position within a custom-designed, air-warmed Plexiglas animal cradle; the head was in the homogeneous B_1 field of an RF coil (copper foil, 4 cm diameter × 4 cm length, mounted on Pyrex glass) [18]. General anesthesia was maintained by delivering nitrous oxide:oxygen gas (1:4 vol/vol, 2 l/min) via face mask to the animal within the Isolette. The cradle allowed the RF coil to be easily and reproducibly located within the most uniform B_0 field of the superconducting horizontal bore magnet (2.0 T). The RF coil at the proton resonance frequency with the animal in position was matched to the impedance of the spectrometer by minimizing the reflected power. Homogeneity of the B_0 field was maximized by prior shimming on a doped water phantom using the air temperature shim gradient coils and the DC offset of the three orthogonal imaging gradient coils. Homogeneity was routinely better than 1 ppm across the head of a rat.

Images were recorded on a Technicare prototype broadband spectrometer equipped with imaging hardware and software. The instrument did not have multislice capabilities. Single-slice coronal images (1.0 mm thick) were obtained after localizing the lesion with the marker over the burr hole on an initial sagittal projectional image. The lesion was located in the coronal plane by moving the whole animal cradle by 1-mm steps until the largest diameter of the lesion was located. Subsequent imaging was performed in this plane. After data acquisition, images were reconstructed, recorded on magnetic tape, and transferred to a Sun Microsystems model 4/260c workstation for production of synthetic images (T1, T2, and line-width) using software developed in our laboratory.

Protocols.—Imaging was performed on rats with lesions of 10–15 weeks in duration. Each animal was imaged with five pulse sequences: (1) SE 2000/50/4 (TR/TE/excitations), (2) ASE 2000/50/5/4 (TR/TE/τ/excitations), (3) SE 400/25/20 (TR/TE/excitations), (4) SE 2000/25/4, and (5) SE 2000/100/4. τ represents the refocusing 180° pulse offset time; the number of acquisitions was varied to maintain equal total acquisition times for all sequences (20 min). A complete description of the implementation of sequence 2 is given elsewhere [16]. The data were acquired as 256 × 128 matrices but displayed as 256 × 256 matrices by interpolation of the phase-encoding data.

In addition to the T2- and T1-weighted images obtained from the above sequences, synthetic images based on line width, T1, and T2 were calculated on a pixel-by-pixel basis by using the following algorithms. These calculated parameters are readily compared between different animals and at different times, whereas signal intensities obtained directly from the initial images are subject to variation on different days and between different animals due to variation in the sensitivity of the imaging system.

Line-width (LW) images were calculated from SE and ASE images assuming Lorentzian line shape (of the general form of $y = 1/$

$[1 + x^2]$) and TE >> τ, using the algorithm discussed in detail elsewhere [16]:

$$LW = [1/(\pi T_2^*)] = (1/\pi\tau)\ \ln(S2/S1) \quad (1)$$

where S1 and S2 are the pixel signal intensities from sequences 1 and 2, respectively. The line width of a pixel is a measure of the spread of resonance frequencies of protons within the pixel. If the pixel corresponds to an area of tissue that shows variation in magnetic susceptibility, such as may arise from the presence of paramagnetic iron storage products, then the resultant magnetic field gradients within the tissue cause dispersion of resonance frequencies of the protons within the pixel. Thus, a large line width means a wide dispersion of frequencies within a pixel, implying the presence of paramagnetic substances and resultant magnetic susceptibility effects.

T1 images were calculated assuming a steady-state solution to the linearized Bloch equations for the saturation recovery SE experiment [19] with a correction for the effect of gaussian slice selection [20] using the equation:

$$SI \propto M_0 e^{-(TE/T2)}(1 - 2e^{-(TR-TE/2)/T1} + e^{-(TR/T1)})(1 - 0.279e^{-(0.78TR/T1)}) \quad (2)$$

This expression for signal intensity, SI, was used to generate a look-up table of the ratio of signal intensities for sequences 3 and 4 for T1 values within physiologic ranges (0 < T1 < 3000 msec). Sequences 3 and 4 were used, as the TE is the same for both short and long TRs, respectively. Cubic spline interpolation, a routine mathematical method of interpolating between data points using a cubic polynomial [21], was performed to improve the precision of the look-up table. The images were then processed by computing the ratio of signal intensities from sequence 3 and sequence 4 on a pixel-by-pixel basis and using that value to determine T1 from the look-up table.

T2 images were computed from pixel signal intensities and the TEs, TE(4) and TE(5), respectively, of images obtained from sequences 4 and 5 (S4 and S5), respectively, assuming a single exponential decay and using the equation:

$$T2 = [TE(5) - TE(4)]/[\ln(S5/S4)] \quad (3)$$

The calculations were performed on a Sun Microsystems workstation (model 4/260c) using software designed to take data from corresponding pixels of any two designated images and calculate the desired parameter using one of the above equations. The result is recorded in an identical-sized matrix that is then displayed as the synthetic image.

Histopathology

Tissue preparation.—For the histochemical staining series, rats were sacrificed at about 1-week intervals from 2 to 15 weeks and the brains removed in toto and fixed overnight at 4°C in a solution of 10% neutral buffered formalin. After cryoprotection in 20% glycerol and 2% dimethyl sulfoxide, each brain was blocked and sectioned in the coronal plane at 50-μm intervals on a freezing microtome. Standard surface landmarks were used to select serial sections spanning the entire basal ganglia. These were collected in sets for storage at 4°C in 0.1 mol/l of phosphate buffer until staining.

Staining procedures.—Alternate sections from each rat brain were stained using the two stains for each iron-storage protein. Although counterstains were used in initial studies, they were not used in the studies employing digitization.

For Perls Prussian blue, the serial sections in the set were mounted on chrome alum–gelatin covered slides and air-dried, followed by immersion in a fresh incubating solution consisting of equal parts of 2% potassium ferrocyanide and 2% hydrochloric acid for 10–60 min [22]. After the reaction was completed, the slides were washed in water and dehydrated, cleared, and applied with cover glasses.

For ferritin immunocytochemistry, free-floating sections were treated in 0.3% hydrogen peroxide in absolute methanol for 30 min followed by 3- to 10-min washes in 0.1 mol/l phosphate-buffered solution (PBS, pH 7.3). After incubation in 10% normal goat serum in PBS to saturate nonspecific antibody binding sites, sections were placed in primary antiserum diluted in PBS with 0.3% Triton-X 100 at room temperature (1:1000, Boehringer Mannheim, rabbit anti-human ferritin). After further PBS washes, the sections were incubated in goat anti-rabbit peroxidase complex (antibody to the rabbit ferritin-specific antibody that is linked to the enzyme peroxidase used to produce the color reaction) for 3 hr (1:200 in PBS, Boehringer Mannheim) followed by further washes and disclosure using 3-3′-diaminobenzidine as the chromogen.

Digitization.—Pathology sections were digitized by using an Eikonix CCD camera (model 1000, 4096 diodes in a linear array × 4096 lines of resolution for a maximum of 4096 × 4096 resolution) interfaced to an IBM PC XT 286 computer that was connected to a network of Sun workstations using PC/NFS software. Images of complete brain sections were obtained through a standard 50-mm camera lens using diffused uncollimated incandescent light transmitted through the slide. Calibration of the camera exposure settings was performed with software supplied by the manufacturer, with 0 corresponding to zero light and 255 (the maximum on the eight-bit scale of the camera) corresponding to full transmission of white light.

Counterstains usually applied for direct visualization were not applied to sections used for digitization because, although of different color, they are still digitized to a gray-scale level. This increases the average background signal in a pathology section, decreasing the discrimination of the lesion from the background in the gray-scale image. Such digitized imaging measures the amount of uncollimated polychromatic light transmitted through the pathology specimen. The quantitative relationship between staining characteristics and transmission of light is complex, and is assumed to be a monotonically increasing function. Different stains can be expected to show different responses depending on the absorbance wavelength and filtering properties of the histologic structures detected by each stain. Because of the complexity of these response functions, it was not possible to quantify the amount of a particular substance present but only to delineate its distribution.

Image Analysis

Both MR and histologic images were analyzed with custom-designed software on the Sun Microsystems model 4/260c workstation. After choosing a background signal intensity over the contralateral hemisphere of the brain (be it an MR or pathology image), signal means and standard deviations were calculated. Contours for signal intensities at a given number of standard deviations (2 SD contour data are presented) from the background mean were then selected over the whole brain, including the ipsilateral hemisphere containing the lesion. The areas of the lesion from the different images of the same brain were then compared by using the two-tailed t test for the mean of differences of paired observations. Differences in areas at the $p < .05$ confidence limit for the two-tailed t test were required for statistical significance. Corrections for the differences in pixel sizes between the MR images (0.2 × 0.1 mm) and pathologic images (0.025 × 0.025 mm) and for changes in size of the brain from in vivo to after fixation (28%, $n = 25$) were applied to allow the areas of signal abnormalities in the various images to be compared directly. Because more data were available for the separate cohorts of animals used for MR and pathology studies, measurements of area of lesions defined by MR images (synthetic line-width and T1-weighted and T2-

weighted images) and pathology images (based on different iron stains) were compared by using the two-tailed t test based on the means of the groups of such unpaired observations with the requirement that statistical significance be reached at the $p < .05$ confidence limit. Registration of thin pathologic sections with considerably thicker MR images makes multiple pathologic sectioning essential for statistical reliability. Pathology sections with maximum lesion size were used for digitization and correlation.

Biochemistry

Tissue preparation.—To ensure that the iron products observed by the histochemical stains were due to injected blood and not just the result of the trauma of injection, and to determine the rate of removal of iron-storage products from the lesion area, iron assays were performed on the series of rats underoing biochemical assay. The concentration of iron remaining in the brains was determined at about 7-day intervals from 3 to 15 weeks after injection of blood ($n = 1$ or 2 for each interval; total, $n = 14$) and plasma ($n = 1$ or 2 for each interval; total, $n = 10$). After sacrifice under general anesthesia, the intact brain was rapidly removed and the lesion was removed in a 3-mm-thick coronal section using standard brain landmarks for localization. The tissue (≈60 mg) around the lesion and that from the corresponding contralateral caudate nucleus (used as an internal control) were harvested separately, washed in cold normal saline, homogenized in phosphate buffer (1 ml, 10 mmol/l, pH 7.2) using a Dounce homogenizer (0.75 or 0.40 ml, 20 plunges), and stored in sealed vials at −5°C prior to assay.

Assays.—Iron analyses were performed by standard colorimetric methods (Sigma Chemical Co. kit #565). Acid digestion (perchloric acid:homogenate:buffer, 0.02:0.050:0.10 ml at 110°C overnight) was required to release protein-bound iron. All assays were performed by using three-point standard curves in triplicate. The total protein of the samples was determined by using standard protein assay techniques (Sigma Chemical Co. kit #690), with five-point standard curves in triplicate. Results were recorded as micromoles iron per mg protein.

Results

Representative contiguous pathology sections for the ferritin and Perls stains at the same magnification in the chronic phase of hematoma resolution (10 weeks) in the same rat demonstrated the presence of two iron-storage substances, hemosiderin and ferritin (Fig. 1). Examination of the distribution of the injected blood in the tissue indicated that the blood dissected along white-matter tracts and along the injection tract extending away from the injection site. This resulted in the elongated distribution observed in Figure 1. Whereas the hemosiderin was localized to macrophages along the injection tract, ferritin appeared not only in macrophages but also in glial cells with a wider distribution from the lesion. The differences in distribution were apparent visually; lesion areas from contiguous sections for the two stains that were 2 SD above background in the digitized pathology images (Fig. 2) are analyzed in Table 1. Because no statistically significant differ-

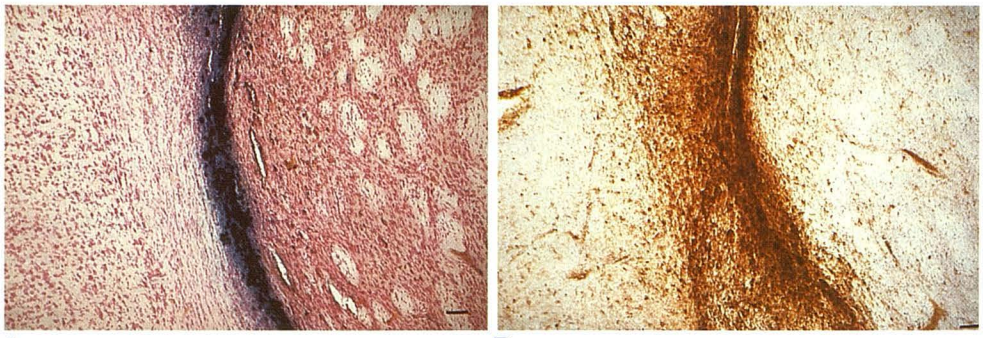

Fig. 1.—Representative pathology stains of contiguous coronal sections at same magnification in same rat brain 10 weeks after injection of blood into right basal ganglia. Scale bar = 0.05 mm.

***A*, Perls Prussian blue stain shows hemosiderin as very dark blue, linear region confined to center of field on lighter background.**

***B*, Immunochemical stain for ferritin shows ferritin as brown on pale background.**

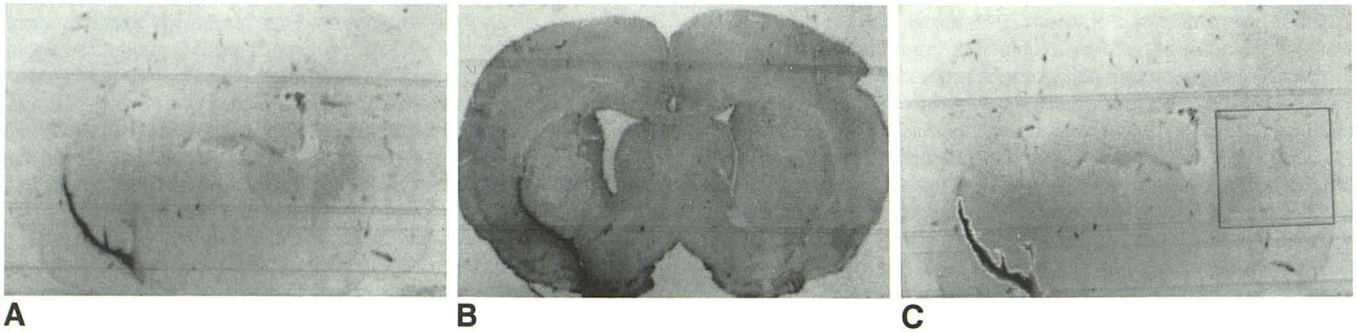

Fig. 2.—*A* and *B*, Digitized images of contiguous coronal brain sections stained for hemosiderin (Perls stain) (*A*) and ferritin (immunochemical stain) (*B*).

***C*, Contour analysis of image in *A* shows region of interest over normal left hemisphere (*black box*) and 2-SD contour about hematoma in right basal ganglia (*white border*). Lesion area is determined from number of pixels within contour multiplied by pixel size and corrected for shrinkage during processing.**

ences could be detected between smaller groups of lesions aged 1–4, 5–9, and 10–15 weeks, these data are pooled in Table 1. Similarly, no difference between venous and arterial blood was detected on MR or pathology images over this time period; thus, these groups were combined for subsequent statistical analysis. Ferritin detected by immunochemical reactivity showed a statistically significant ($p < .01$ for blood injection, $p < .05$ for plasma injection) broader distribution than hemosiderin detected by Perls stain positivity for contour thresholds of 2 SD above background. The lesions created by plasma injection contained significant iron-storage products, as detected by the stains, but the area of hemosiderin distribution was statistically greater in the blood-injected lesions ($p < .01$).

Biochemical analysis of the concentration of total iron as summarized in Table 2 demonstrated that both the plasma- and blood-injected lesions showed a statistically significant increased level of iron above the background in the contralateral hemisphere ($p < .01$) and that the blood-injected lesions contained more iron than the plasma-injected lesions ($p < .01$). No statistically significant variation in the quantity of iron was found from 1 to 15 weeks, suggesting that iron recycling away from the lesion was very slow over this time period.

Comparison of areas of lesions on T1- and T2-weighted SE images demonstrated that the areas of signal change at contour thresholds of 2 SD above background are significantly greater for T2- than for T1-weighted images ($p < .01$), with no statistical difference between the blood- and plasma-injected groups.

Representative SE, ASE, and line-width images are presented in Figure 3. The larger area of signal loss in the right basal ganglia on the ASE image (Fig. 3B) relative to the SE

TABLE 1: Comparison Among Areas of Late-Phase Hematomas Detected by Line-Width MR Images and Measured from Digitized Pathology Images of Brain Sections Stained for Ferritin Immunoreactivity and Perls Positivity

Lesion Group	Mean Area (mm^2)			Significance (p)		
	Ferritin (n)	Perls Stain (n)	Line Width (n)	Ferritin–Perls	Line Width–Ferritin	Line Width–Perls
Blood	16 ± 7 (9)	6 ± 2 (9)	12 ± 8 (8)	<.01	NS	<.05
Plasma	11 ± 8 (9)	3 ± 2 (9)	9 ± 2 (2)	<.05	NS	<.01
Significance (blood-plasma)	NS	<.01	NS	–	–	–

Note.—Areas were determined within contour thresholds of 2 SD above backgrounds. Statistical significance was determined by two-tailed t test for the paired ferritin-Perls observations and for means of separate cohorts of rats for the unpaired observations. NS = not significant at the .05 confidence limit.

TABLE 2: Biochemical Analysis of Iron in Ipsilateral (Right) and Contralateral (Left) Basal Ganglia of Rats with Late-Phase Hematomas Produced in Right Basal Ganglia

Lesion Group	Mean Iron Content (μg/mg protein)		Right-Left Significance (p)
	Right Hemisphere	Left Hemisphere	
Blood ($n = 14$)	0.8 ± 0.4	0.3 ± 0.1	<.01
Plasma ($n = 10$)	0.4 ± 0.2	0.2 ± 0.1	NS
Significance (blood-plasma)	<.01	NS	–

Note.—Statistical significance was determined by two-tailed t test for means of unpaired observations. NS = not significant at the .05 confidence limit.

Fig. 3.—Representative in vivo coronal images of rat brain 10 weeks after production of hematoma.
***A*, Symmetric SE 2000/50/4 sequence.**
***B*, Asymmetric SE 2000/50/4 sequence ($\tau = 5$).**
***C*, Synthetic line-width image calculated from symmetric and asymmetric SE images with the use of equation 1 in text.**

image (Fig. 3A) was due to the greater sensitivity of the ASE image to magnetic susceptibility effects, as is discussed elsewhere [16]. The area of increased line width on the line-width image reflected the areas of both the SE and ASE images, and hence shows an area similar to that on the ASE image. The line widths of individual pixels at the center of the lesion were as high as 3–4 ppm, as compared with less than 0.2 ppm in normal tissue. This indicates significant magnetic susceptibility effects in the area of the lesion. Because line-width images are based on signal ratios, systematic changes in signal intensities across the images (caused by B_1 inhomogeneities) are corrected, thereby making contour mapping more reliable. Therefore, the contour analysis of lesions on line-width maps allowed more straightforward comparisons with pathology images than did the T1- or T2-weighted images obtained directly from the SE 400/25/20 and SE 2000/50/4 sequences, respectively. The areas of change in line width on line-width images, and ferritin stain immunoreactivity and Perls stain positivity on pathology images, are compared in Table 1 for blood and plasma lesions. Whereas the areas determined from line-width changes and ferritin immunoreactivity were not statistically different, the area of Perls positivity was significantly smaller ($p < .05$ for blood, $p < .01$ for plasma). These data showed no difference in areas in line-width changes and ferritin immunoreactivity between plasma- and blood-injected lesions, whereas the area of Perls positivity increased with blood injection ($p < .01$).

The signal-to-noise ratio of the synthetic T1 and T2 images was of insufficient quality to permit reliable contour analysis of lesion areas. However, our visual inspection of representative images showed that T1 changes were not readily detected, whereas T2 changes were observed in the area of the lesion.

Discussion

The lesions produced in the rat model of late hematoma showed stability in biochemical forms and area of distribution of iron-storage products within the statistical limits measured in this study over the 2- to 15-week period. Such stability may reflect the rapid establishment of the blood-brain barrier after initial traumatic disruption with consequently slow recycling of iron back to the reticuloendothelial system. The long-term deposition of hemosiderin in human cerebral hemorrhage is well documented and is in marked contrast to extraaxial lesions not contained by a blood-brain barrier [1]. As iron products were detected in both blood- and plasma-injected lesions, some of the iron must arise from local bleeding caused by the trauma of the injection. This is not surprising, as morphologic changes showed that the injected fluid dissected along white-matter tracts of the internal capsule rather than forming a discrete spherical hematoma. Such patterns are observed in arterial putaminal hemorrhages in humans. As heparin was used in the preparation of the plasma, traumatic bleeding may have been more pronounced in the plasma-injected lesions. Nevertheless, based on the distribution analysis of this study, the excess iron introduced by injection of blood rather than plasma increased the area of hemosiderin but not of ferritin. This suggests that this deposited blood may constitute a localized iron overload state, overloading the supply of apoferritin with concomitant formation of hemosiderin. Although the wider distribution of ferritin relative to hemosiderin may reflect the increased sensitivity of the immunochemical ferritin stain over that of the Perls stain, the differential increase in area of hemosiderin without change in ferritin between blood and plasma groups cannot be explained by stain sensitivity. Similarly, although the background of the ferritin stain is greater than that of the Perls stain, the analysis of digitized pathology images at statistically well-defined contour thresholds above background ensures that background bias is avoided.

Comparison of the areas of line broadening from magnetic susceptibility effects of the iron-storage substances on line-width MR images with areas of lesions defined by the pathology images suggests that the area of significant line broadening matches the wider distribution of ferritin rather than hemosiderin. Similarly, the constancy of the distribution of ferritin and line-width changes for blood and plasma injections, in contrast to the corresponding increase in the area of hemosiderin, supports this contention. However, quantitative biochemical fractionation of ferritin and hemosiderin is still required to determine the relative contributions of these two substances to the heterogeneity of tissue magnetic susceptibility.

This study suggests that the current explanation for the MR appearance of late-phase cerebral hematoma proposed by Gomori and Grossman [1] may require modification to include the role of ferritin in addition to hemosiderin as a source of magnetic susceptibility effects, as summarized in Figure 4. Human studies are essential to establish the relevance of this finding to clinical studies.

The marked signal changes on T2-weighted and T2 images, which are not readily apparent on T1-weighted and T1 images, demonstrate the presence of magnetic susceptibility–induced T2 relaxation with minimal relaxivity effects from dipole-dipole–induced T1 relaxation. Lack of the short-range relaxivity effects is expected for aggregates of iron-storage proteins such as ferritin and hemosiderin within subcellular compartments in which water is restricted from close approach to the paramagnetic and perhaps superparamagnetic

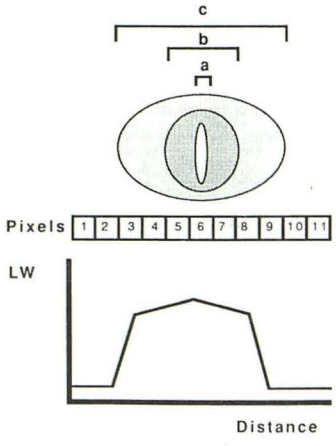

Fig. 4.—Schematic diagram of late phase of resolving hematoma as determined in rat model in which central cavitation (a) is variably present and surrounded by inner area of macrophages containing ferritin and hemosiderin (b) and wider area of ferritin in glial cells (c). Line width (LW) is increased in pixels (3 to 9) covering distribution of ferritin (c) but remains within normal limits (<0.2 ppm) outside this area.

ferric ions. However, diffusion of water through the magnetic field inhomogeneities induced by the volumes of different magnetic susceptibility, such as paramagnetic iron aggregates in surrounding diamagnetic tissue within a single imaging voxel, is significant during the TE time of T2-weighted imaging. Such diffusion results in signal attenuation. This mechanism is verified directly by the increase in line width on the line-width images.

As predicted from the known pathways of iron metabolism, at least two iron-storage substances are present in the late phase of resolution of cerebral hematoma. Ferritin in glial cells and macrophages has a wider distribution than hemosiderin in macrophages around the lesion. The rat model has provided a simple model for comparison of histopathology, biochemistry, and MR imaging data. The use of digitized histopathology provides an objective means of quantifying lesion size as depicted by specific stains for comparison with areas of signal changes on MR images. The use of line-width images in addition to T1- and T2-weighted images allows signal changes in late-phase hematomas to be attributed to intravoxel magnetic field inhomogeneities that show a distribution similar to that of ferritin. The late phase of hemorrhage described by the model of Gomori and Grossman [1] should be modified to include the role of ferritin in the magnetic susceptibility–induced signal changes observed in MR images. Determination of the relative contributions of ferritin and hemosiderin to such magnetic susceptibility effects awaits quantitative biochemical fractionation of these substances.

ACKNOWLEDGMENTS

We thank Edward P. Richardson for his enthusiasm and encouragement and Richard B. Buxton for his method of calculating T1 values.

REFERENCES

1. Gomori JM, Grossman RI. Head and neck hemorrhage. In: Kressel HY, ed. *Magnetic Resonance Annual 1987*. New York: Raven, **1987**:71–112
2. Sipponen JT, Sepponen RE, Silvula A. Nuclear magnetic resonance (NMR) imaging of intracerebral hemorrhage in the acute and resolving phases. *J Comput Assist Tomogr* **1983**;7:954–960
3. DeLaPaz RL, New PFJ, Buonanno FS, et al. NMR imaging of intracranial hemorrhage. *J Comput Assist Tomogr* **1984**;8:599–607
4. Di Chiro G, Brooks RA, Girton ME, et al. Sequential MR studies of intracerebral hematomas in monkeys. *AJNR* **1986**;7:193–199
5. Gomori JM, Grossman RI, Goldberg HI, Zimmerman RA, Bilaniuk LT. Intracranial hematomas: imaging by high-field MR. *Radiology* **1985**;157:87–93
6. Gomori JM, Grossman RI, Hackney DB, Goldberg HI, Zimmerman RA, Bilaniuk LT. Variable appearances of subacute intracranial hematomas on high-field spin-echo MR. *AJNR* **1987**;8:1019–1026
7. Gomori JM, Grossman RI, Hackney DB, et al. Acute intracranial hemorrhage: intensity changes on sequential MR scans at 0.5 T. *AJNR* **1988**;9:47–57
8. Edelman RR, Johnson KA, Buxton RB, et al. MRI of hemorrhage: a new approach. *AJNR* **1986**;7:751–756
9. Trump BF, Valigorsky JM, Arstila AU, Mergner WJ, Kinney TD. The relationship of intracellular pathways of iron metabolism to cellular iron overload and iron storage diseases. *Am J Pathol* **1973**;72:295–324
10. Hill JM, Switzer RC. The regional distribution and cellular localization of iron in the rat brain. *Neuroscience* **1984**;11:595–603
11. Deizel PB. Iron in the brain: a chemical and histochemical examination. In: Waelsch H, ed. *Biochemistry of the developing nervous system*. London: Academic Press, **1955**:145–152
12. Drayer B, Burger P, Darwin R, Riederer S, Herfkens R, Johnson GA. Magnetic resonance imaging of brain iron. *AJNR* **1986**;7:373–380
13. Matsuno T, Mori M, Awai M. Distribution of ferritin and hemosiderin in the liver, spleen and bone marrow of normal, phlebotomized and iron overloaded rats. *Acta Med Okayama* **1985**;39:347–360
14. Lauffer RB. Paramagnetic metal complexes as water proton relaxation agents for NMR imaging: theory and design. *Chem Rev* **1987**;87:901–927
15. Thulborn KR, Brady TJ. Iron in magnetic resonance imaging of cerebral hemorrhage. *Magn Reson Q* **1989**;5:23–38
16. Wismer GL, Buxton RB, Rosen BR, et al. Susceptibility induced magnetic resonance line broadening: applications to brain iron mapping. *J Comput Assist Tomogr* **1988**;12:259–265
17. Konig JRF, Klippel RA. *The rat brain: a stereotaxic atlas of the forebrain and lower parts of the brain stem*. Baltimore: Williams & Wilkins, **1963**
18. Hoult DH. The NMR receiver: a description and analysis of design. *Prog NMR Spectra* **1978**;12:41–77
19. Farrar TC, Becker ED. *Pulse and Fourier transform NMR*. New York: Academic Press, **1971**:1–65
20. Buxton RB, Wismer GL, Brady TJ, Rosen BR. Quantitative proton chemical shift imaging. *Magn Reson Med* **1986**;3:881–900
21. Press WH, Flannery BP, Teukosky SA, Vetterling WT. *Numerical recipes in C. The art of scientific computing*. Cambridge, England: Cambridge University, **1988**:94–98
22. Luna L. *Manual of histologic staining methods of the armed forces institute of pathology*. New York: McGraw-Hill, **1968**